Research Article

Orthorectification of WorldView-3 Satellite Image Using Airborne Laser Scanning Data

Biswajeet Pradhan [1,2] **Ahmed A. Ahmed,** [1] **Subrata Chakraborty** [1] **Abdullah Alamri,** [3] **and Chang-Wook Lee** [4]

[1]*Centre for Advanced Modelling and Geospatial Information System (CAMGIS), Faculty of Engineering and IT, University of Technology, Sydney, NSW 2007, Australia*
[2]*Earth Observation Center, Institute of Climate Change, Universiti Kebangsaan Malaysia, 43600 UKM, Bangi, Selangor, Malaysia*
[3]*Department of Geology and Geophysics, College of Science, King Saud University, P.O. Box 2455, Riyadh 11451, Saudi Arabia*
[4]*Division of Science Education, Kangwon National University, Kangwondaehak-gil, Chuncheon-si, Gang-won-do 24341, Republic of Korea*

Correspondence should be addressed to Biswajeet Pradhan; biswajeet24@gmail.com

Satellite images have been widely used to produce land use and land cover maps and to generate other thematic layers through image processing. However, images acquired by sensors onboard various satellite platforms are affected by a systematic sensor and platform-induced geometry errors, which introduce terrain distortions, especially when the sensor does not point directly at the nadir location of the sensor. To this extent, an automated processing chain of WorldView-3 image orthorectification is presented using rational polynomial coefficient (RPC) model and laser scanning data. The research is aimed at analyzing the effects of varying resolution of the digital surface model (DSM) derived from high-resolution laser scanning data, with a novel orthorectification model. The proposed method is validated on actual data in an urban environment with complex structures. This research suggests that a DSM of 0.31 m spatial resolution is optimum to achieve practical results (root-mean-square error = 0.69 m) and decreasing the spatial resolution to 20 m leads to poor results (root-mean-square error = 7.17). Moreover, orthorectifying WorldView-3 images with freely available digital elevation models from Shuttle Radar Topography Mission (SRTM) (30 m) can result in an RMSE of 7.94 m without correcting the distortions in the building. This research can improve the understanding of appropriate image processing and improve the classification for feature extraction in urban areas.

1. Introduction

Increased availability of high-resolution satellite images is driving the rapid expansion in remote sensing applications, including commercial, industrial, governmental, and research domains [1–10]. High-resolution satellite images are also commonly used in urban remote sensing applications, such as change detection, urban sprawl, land use/land cover mapping, environmental studies, and transportation [5–7].

Terrain distortions in satellite imagery off-nadir angle data acquisition require sophisticated data preprocessing algorithms to obtain useful data for these applications. The effect of relief displacement on off-nadir satellite images causes difficulty in accurately extracting features in urban areas surrounded by high-rise buildings. Joshi et al. [2] and Peng et al. [6] suggested that using elevation data or multiple images acquired from different angles in remote sensing applications, such as image classification, building detection, and city modeling, is preferable. These problems originated from the reduced pixel dimensions and off-nadir viewing. One approach to correct such geometric errors in satellite images is called orthorectification, which is the adjustment of a perspective image geometrically to an orthogonal image by transforming the coordinates from an image to the ground spaces and removing relief displacements and tilt.

Different from other terrain correction methods, which depend on the horizontal position of image pixels [11], orthorectification considers the pixel positional shift caused by the earth's curvature and provides actual ground coordinates (X, Y, and Z values) for all pixels. Orthorectification requires a digital elevation model (DEM) and ground control points (GCPs). The DEM can be obtained from a variety of sources with various resolutions, such as Radarsat-1 and Light Detection and Ranging (LiDAR) data [12].

Several techniques and algorithms have been developed to improve the orthorectification processes and decrease the distortions resulting from these processes. Belfiore and Parente [13] compared different methods, including polynomial functions and rational functions, for correcting deformations of WorldView-2 satellite images with a variable number of GCPs. The rational functions were more suitable than the other techniques for correcting deformations in WorldView-2 images. Prakash et al. [14] proposed an inverse orthorectification method, which utilizes road data and DEM to correct geometric deformations in satellite images. These methods showed acceptable accuracy and improved the road feature extraction from satellite images. Alrajhi et al. [15] developed an automatic procedure that can orthorectify high-resolution satellite images with no GCPs and can respond to real-time geospatial data updates. Furthermore, Whiteside and Bartolo [16] investigated orthorectified images with the aid of the sensor's rational polynomial coefficients (RPCs) and GCPs using differential global positioning system (DGPS) with an accuracy of 10 cm. Zhang et al. [1] proposed a new method for integrated PCI-RPC and ArcGIS-Spline tools for orthorectification in satellite images. The integrated approach improved the RMSE accuracy from 2.94 m to 1.10 m. Henrico et al. [15] developed an orthorectification process based on high-quality 2 m DEM and applied two different GCP collection methods. First, field survey method with the aid of DGPS was adopted. In the second method, TerraSAR-X-based GCPs were acquired from Airbus Defense and Space. The manual GCPs yielded better positional orthoimages than the TerraSAR-X-based GCPs [17, 18].

The above literature review shows the various orthorectification processing methods. However, many researches confined correction the image geometry based on DEM and DSM data, not on the correcting the buildings distortions of high-resolution satellite images. As a result, the following sections present and discuss a novel orthorectification method designed for WorldView-3 data with a high off-nadir angle. The following important questions are answered: (1) the required resolution of DSM data to obtain practical results and (2) whether or not using high-resolution DSM data instead of the freely available digital elevation models is beneficial or is the latter sufficient for correcting terrain distortions in WorldView-3 imageries.

2. Materials and Methods

2.1. Study Area.
The experiment was conducted in an area located in Selangor, Malaysia, that is geographically bounded between ($101°30'$-$102°0'$) E and ($3°00'$-$3°30'$) N. The study area was carefully selected to successfully achieve our objectives. Various land uses, such as residential, commercial, industrial, public, sport, educational, and religious facilities, and land covers related to human activities are available in the study area, as shown in Figure 1.

2.2. Datasets.
Laser cloud points: point clouds are defined as a set of vertices in a three-dimensional coordinate system, and these clouds add a new type of geometry to the system. Point clouds, as the output of 3D scanning processes, have many purposes, such as creating 3D models for multitude visualization, rendering, animation, and mass customization applications. In this research, airborne LiDAR point clouds were used to create an extremely high-resolution DEM and digital surface model (DSM), as shown in Figure 2. The LiDAR data were gathered by using an airborne system (Optech Airborne Laser Terrain Mapper 3100) on November 2, 2015. The camera had a spatial resolution of 10 cm; the laser scanner had a scanning angle of 60° with a camera angle of ±30° and the flying height of 1510 m with clear skies. The posting density of the LiDAR data was 3–4 pts/m² (average point spacing = 0.30 m) with a 25,000 Hz pulse rate frequency. The number of points is 1,300,000 points for the study area.

WorldView-3: the WorldView-3 satellite image showed eight bands of panchromatic spatial resolution, multispectral, short-wave infrared, and Clouds, Aerosols, Vapours, Ice, and Snow (CAVIS) resolution at 0.31, 1.24, 3.7, and 30 m, respectively. The four standard VNIR colours were blue, green, red, and near-infrared, and the additional VNIR colours were coastal, yellow, red edge, and near-IR2. Twelve (12) CAVIS bands (atmospheric sensor) were used, and the off-nadir angle was 14°. The data were gathered on April 25, 2015.

2.3. Methodology.
Figure 3 shows the methodology adopted in this research using orthorectification and involves an indirect method. The indirect method requires building the RPC model to derive at least four GCPs from DEM 30 cm. A total of 55 GCPs, which were derived from DEM of 30 cm, were used. Orthorectification was applied through ArcGIS application to process the oblique images of tall buildings. Moreover, global mapper software was used to process the LiDAR data, whereas ENVI was used to build the RPCs, radiometric calibration, geometric calculations, and filtering. Pan-sharpening was responsible for merging high-resolution panchromatic and low-resolution multispectral images of the WorldView-3 to produce a high-resolution colour image.

Data preparation: two distinct datasets are prepared for this study.

(1) LiDAR data processing: it consists of multiple steps, beginning with LiDAR georeferencing. It is defined by transforming the LiDAR data coordinate system to the Universal Transverse Mercator projection and the world geodetic system 1984 datum by using Global Mapper. The LiDAR data are classified based on the multiscale curvature classification (MCC)
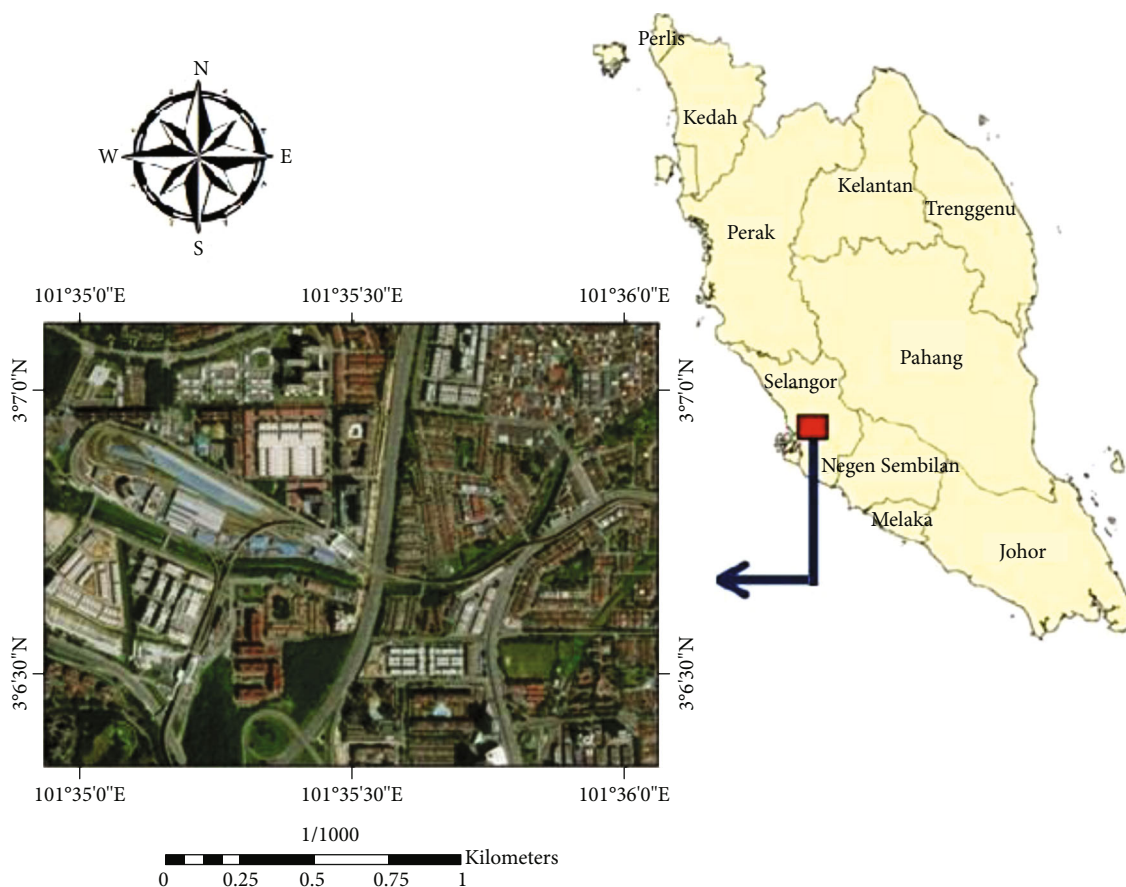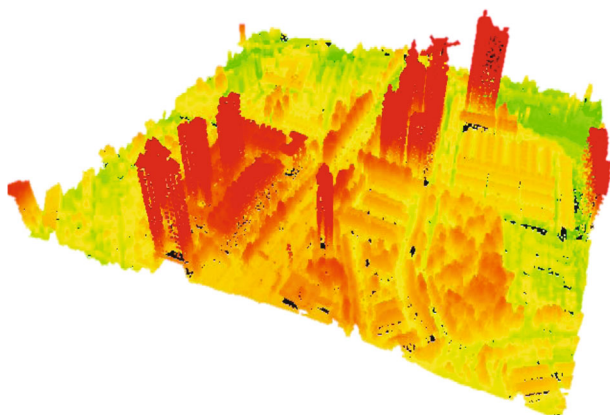
FIGURE 1: Study area map.

FIGURE 2: LiDAR point clouds representing the study area.

method [11] to classify the data into ground points and nonground points. Filtering is then applied to remove existing noise from the cloud points. However, the LiDAR data derived from DEM and DSM were created based on the point clouds with extension LAS by using the ArcGIS application. The multiscale curvature classification (MCC) algorithm was applied to classify the LiDAR returns to the ground and nonground points. The algorithm incorporated

curvature filtering with a scale component and variable curvature tolerance. A surface was interpolated at different resolutions using the thin-plate spline method [19], and the points were classified based on a progressive curvature threshold parameter. The curvature tolerance parameter increased as resolution coarsened to compensate for the slope effect because the data were generalized. Moreover, the DEM applied was 0.31 m, and the DSM values were 0.31, 0.5, 1, 3, 5, 10, 15, and 20 m

(2) WorldView-3 image processing: this requires calibration because the spectral data acquired by the satellite sensors are influenced by several factors, such as sensor calibration, atmospheric absorption and scattering, sensor-target-illumination geometry, and image calibration, and these factors tend to change overtime. Therefore, radiometric correction must be performed by detecting actual landscape changes, as revealed by the changes in surface reflectance from multidate satellite images. After image calibration, we used and applied the pan-sharpening tool to merge the WorldView-3 panchromatic image (31 cm) with WorldView-3 multispectral image (1.24 m) to produce a high resolution of 31 cm with eight bands. This process involves producing a single high-resolution colour image by merging high-
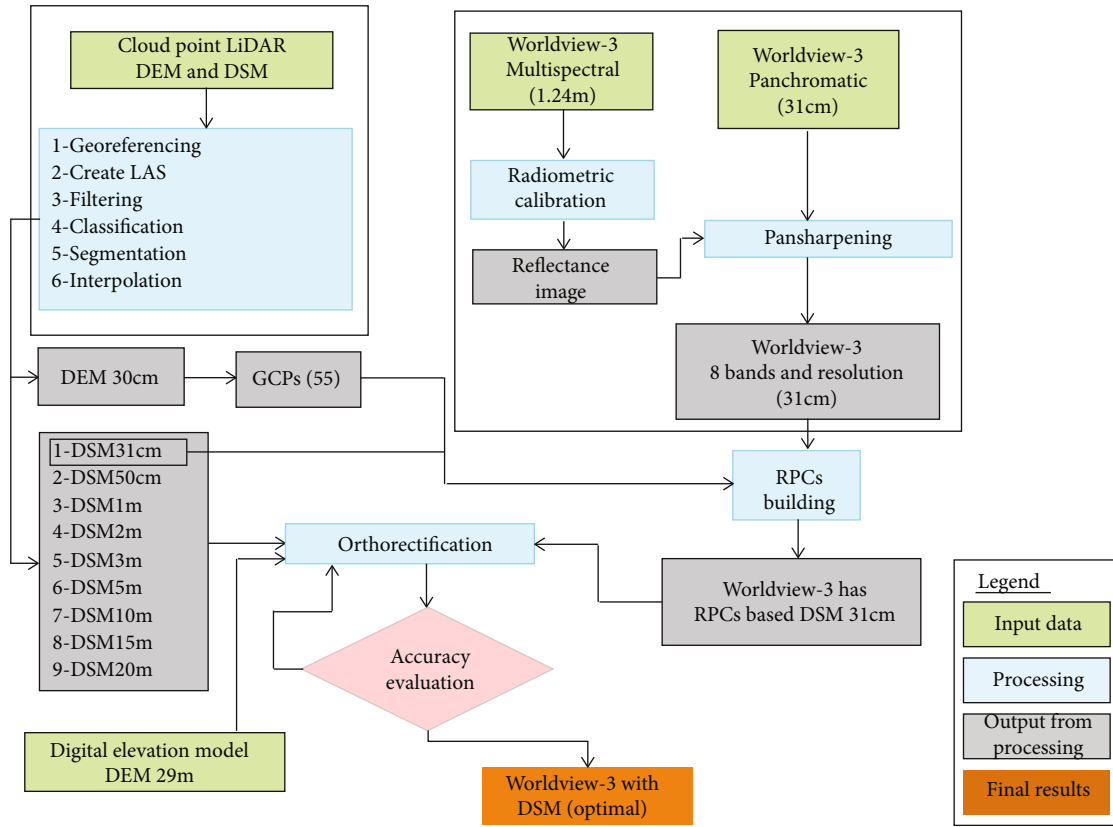
FIGURE 3: Methodology used in this study.

(a)   (b)
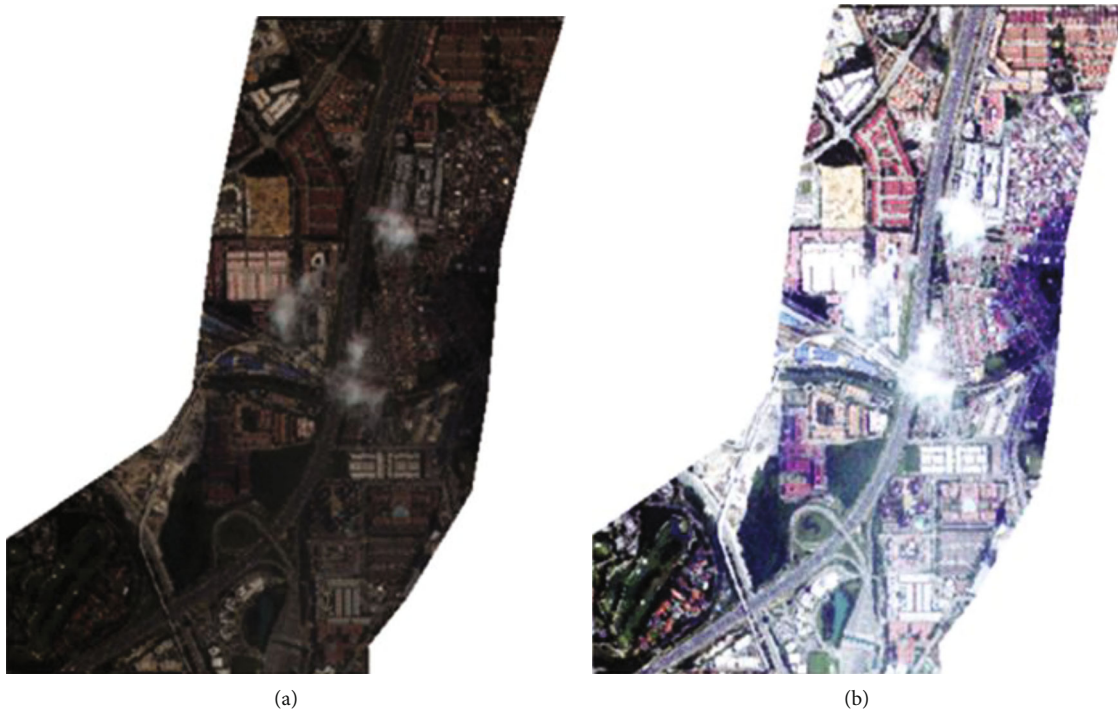
FIGURE 4: WorldView-3 after calibration and pan-sharpened process (a) before and (b) after.

FIGURE 5: GCP distribution on DEM raster.

resolution panchromatic and lower-resolution multi-spectral images. The benefit of this process is to obtain multispectral resolution with high-spatial resolution. Figure 4 shows the WorldView-3 image, before and after results of the processing

Orthorectification model: the modeling involves three key stages.

(1) GCP collection: GCP collection is required for orthorectification. In this study, the GCP data were acquired through a very high-resolution DEM (31 cm) based on LiDAR [12]. During orthorectification, 55 points were used in the area under consideration. Each GCP was situated on easily identifiable objects in the image that can be obtained in the field. It is positioned in the angle of the identified objects displayed in high contrast; the objects are usually artificial, such as bridges, street corner, and buildings. But in this study, we focused on the distortion building which the number of the distortion building is 43 in this study, so we added the GCP on these buildings as shown in Figure 5

(2) Rectification model with RPC: Grodecki and Dial [20] reported that the RPC model is developed based on GCPs and DEM data to orthorectify images. This model is superior to the sensor model used to acquire lines and rows of images by using the ratio of two polynomial functions, which are functions of the ground coordinates. Nichol et al. [21] inferred that the RPC model is developed to generalize the polynomial and linear transform model, which is appropriate for different sensor types. In the RPC rectification model, the image coordinates are the

ratios of two polynomials, in which the three-dimensional coordinates of GCPs are set as independent variables, as shown in

$$\left(r_n = \frac{P_1(X_n, Y_n, Z_n)}{P_2(X_n, Y_n, Z_n)} \right), \tag{1}$$

$$\left(c_n = \frac{P_3(X_n, Y_n, Z_n)}{P_4(X_n, Y_n, Z_n)} \right), \tag{2}$$

where (r_n, c_n) and (X_n, Y_n, Z_n) are the normalized image coordinates (r, c) and ground coordinates (X, Y, Z), respectively, derived from translating and scaling the RPC model.

$$\left(X_n = \frac{X - X_0}{X_s} \right),$$

$$\left(Y_n = \frac{Y - Y_0}{Y_s} \right),$$

$$\left(Z_n = \frac{Z - Z_0}{Z_s} \right), \tag{3}$$

$$\left(r_n = \frac{r - r_0}{r_s} \right),$$

$$\left(c_n = \frac{c - c_0}{c_s} \right),$$

where X_0, Y_0, Z_0, r_0, and C_0 represent the translating parameters for standardization, and these parameters are the coordinates of the origin of the RPC model in the mapping coordinate system. X_s, Y_s, Z_s, r_s, and c_s are the proportionality parameters of standardization. In the polynomial, $P_i(X, Y, Z)$ $(i = 1, 2, 3, 4)$ is the maximum, and the sum power of each coordinate component is not greater than three.

$$\begin{aligned} P(X, Y, Z) = {} & a_0 + a_1 X + a_2 Y + a_3 Z + a_4 XY + a_5 XZ + a_6 YZ \\ & + a_7 X_2 + a_8 Y_2 + a_9 Z_2 + a_{10} XYZ + a_{11} X_2 Y \\ & + a_{12} X_2 Z + a_{13} Y_2 X + a_{14} Y_2 Z + a_{15} XZ_2 \\ & + a_{16} YZ_2 + a_{17} X_3 + a_{18} Y_3 + a_{19} Z_3, \end{aligned} \tag{4}$$

where the polynomial coefficients $a_0, a_1, \cdots, a_{19}$ are designated as the coefficients of the rational polynomial function. (2) Orthorectification principle of the RPC model:

$$\left(r = r_s \frac{P_1(X_n, Y_n, Z_n)}{P_2(X_n, Y_n, Z_n)} + r_0 \right),$$

$$\left(c = c_s \frac{P_3(X_n, Y_n, Z_n)}{P_4(X_n, Y_n, Z_n)} + c_0 \right), \tag{5}$$

$$r = rsF(X_n, Y_n, Z_n) + r_0,$$

$$c = csG(X_n, Y_n, Z_n) + c_0.$$
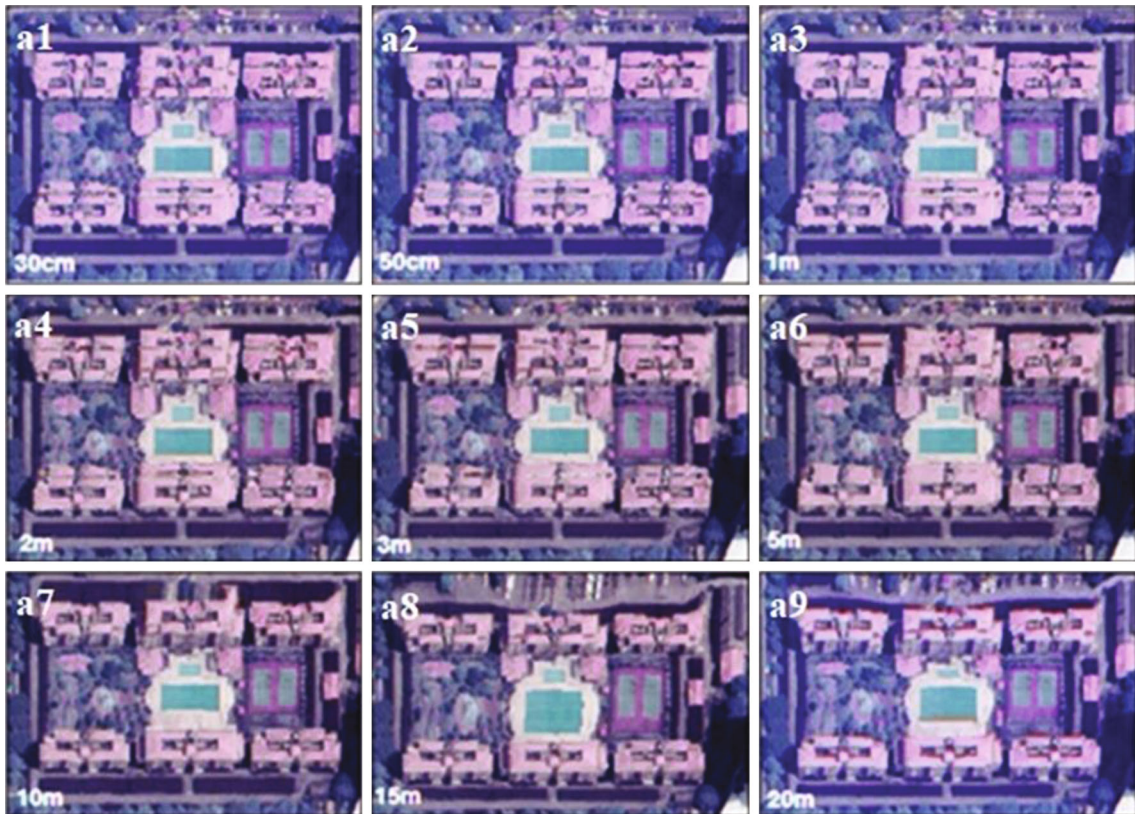
FIGURE 6: Image prior to orthorectification.

FIGURE 7: Image after orthorectification process based on different spatial resolution DSM.

Let $F(X_n, Y_n, Z_n) = (P_1(X_n, Y_n, Z_n))/(P_2(X_n, Y_n, Z_n))$ and $G(X_n, Y_n, Z_n) = (P_1(X_n, Y_n, Z_n))/(P_2(X_n, Y_n, Z_n))$; then, Equation (6) can be rewritten as follows:

$$\begin{cases} r = \dot{r} + \dfrac{\partial_r}{\partial_x}\Delta X + \dfrac{\partial_r}{\partial_y}\Delta Y + \dfrac{\partial_r}{\partial_z}\Delta Z + r_0, \\[2mm] r = \dot{c} + \dfrac{\partial_c}{\partial_x}\Delta X + \dfrac{\partial_c}{\partial_x}\Delta Y + \dfrac{\partial_c}{\partial_x}\Delta Z + c_0. \end{cases} \tag{6}$$

Equation (7) can be represented in Taylor formula format as follows:

$$\begin{cases} \vartheta_r = \begin{bmatrix} \dfrac{\partial_r}{\partial_x} & \dfrac{\partial_r}{\partial_y} & \dfrac{\partial_r}{\partial_z} \end{bmatrix} \begin{bmatrix} \Delta X \\ \Delta Y \\ \Delta Z \end{bmatrix} + (r - \dot{r}), \\[6mm] \vartheta_c = \begin{bmatrix} \dfrac{\partial_c}{\partial_x} & \dfrac{\partial_c}{\partial_y} & \dfrac{\partial_c}{\partial_z} \end{bmatrix} \begin{bmatrix} \Delta X \\ \Delta Y \\ \Delta Z \end{bmatrix} + (c - \dot{c}), \end{cases} \tag{7}$$

$$V = \begin{bmatrix} \vartheta_r \\ \vartheta_c \end{bmatrix},$$

$$A \begin{bmatrix} \dfrac{\partial_r}{\partial_x} & \dfrac{\partial_r}{\partial_y} & \dfrac{\partial_r}{\partial_z} \\ \dfrac{\partial_c}{\partial_x} & \dfrac{\partial_c}{\partial_y} & \dfrac{\partial_c}{\partial_z} \end{bmatrix},$$

$$\Delta = \begin{bmatrix} \Delta X \\ \Delta Y \\ \Delta Z \end{bmatrix},$$

$$l = \begin{bmatrix} +(r - \dot{r}) \\ +(c - \dot{c}) \end{bmatrix}. \tag{8}$$

Lastly, the equation can be modified in a matrix and vector form, as follows:

$$V = A\Delta + l, \tag{9}$$

where $A\Delta$ is a matrix of $\Delta X, \Delta Y, \Delta Z$ representing the ground coordinates (X, Y, Z) and l is the normalized image coordinates.

Tao et al. suggested that the least squares solution of coordinate corrections can be derived from Equation (10), as follows:

$$\Delta = \begin{bmatrix} \Delta X & \Delta Y & \Delta Z \end{bmatrix}^T = A^{-1}(V - 1) = \left(A^T A\right)^{-1} A^{-1}(V - 1). \tag{10}$$

(3) Orthorectification on GIS: orthorectification was applied using GIS tools to produce different orthorectified images that were derived from the integration of very high-resolution image (WorldView-3) and DSM with different accuracies, such as 0.31, 1, 2, 3, 5, 10, 15, and 20 m. The results were compared with one source (WorldView-3) to investigate the optimal image with DSM. Images can be orthorectified by pixel tying to an actual location in 3-dimensional (XYZ) space; orthorectification can be achieved with a mathematical model with RPCs or with a geometric model, which is more or less an internal sensor model; these techniques are called RPC orthorectification and rigorous orthorectification, respectively. Recently, several sensors, including RPCs, with image delivery systems have been used in this regard. Developing a system for images that are not associated with such RPCs is possible if the main properties of internal camera orientation and external environment are known. DEM, automated tie point generation, and a couple of ground control points can facilitate RPC orthorectification accurately

TABLE 1: Summary of residual errors of GCPs for orthoimages (unit: meter).

Warp image and DSM	Orthorectified image	RMSE
WorldView-3 and DSM 31 cm	a_1	0.638
WorldView-3 and DSM 50 cm	a_2	0.764
WorldView-3 and DSM 1 m	a_3	1.302
WorldView-3 and DSM 2 m	a_4	1.718
WorldView-3 and DSM 3 m	a_5	2.106
WorldView-3 and DSM 5 m	a_6	3.26
WorldView-3 and DSM 10 m	a_7	5.529
WorldView-3 and DSM 15 m	a_8	6.501
WorldView-3 and DSM 20 m	a_9	7.175
WorldView-3 and free DEM 30 m	a_{10}	7.947

3. Results and Discussion

3.1. WorldView-3 Image Orthorectification-Based GCPs and LiDAR DSM.
WorldView-3 was orthorectified to the final orthoimage using the above-referenced method in Figure 6. The results are presented as nine images with different accuracies based on varying DSM resolutions (i.e., 31 cm, 50 cm, 1 m, 2 m, 3 m, 5 m, 10 m, 15 m, and 20 m) and GCPs, as shown in Figure 7.

3.2. Accuracy Assessment.
Table 1 presents the results of the minimum, maximum, and the root-mean-square error (RMSE) of orthorectified images based on different DSM resolutions with respect to the GCPs. The horizontal accuracy of the orthorectified images is evaluated based on RMSE error value obtained by computing changes in the coordinate object at a very high-resolution DEM of 31 cm to the coordinate object in the orthoimage result. Equations (1), (2), and (3) [22] are used to determine the RMSE for X and Y coordinates and RMSE horizontal (X, Y), respectively.

$$\text{RMSE} = \sqrt{\frac{\sum_{i=1}^{n}(|x\,\text{input} - x\,\text{control}|)^2 + (|y\,\text{input} - y\,\text{control}|)^2}{n}}. \tag{11}$$

X and Y inputs represent the coordinates of the orthoimage WorldView-3 and X control; Y control represents the coordinates of the intensity of the DEM at 31 cm reference points. The parameters n and i represent the checkpoints tested for an integer between 1 to n, respectively. Table 1 indicates that the RMSE was 0.638 at DSM value of 31 cm. This value increased to 0.764 when the DSM resolution increased to 50 cm. A consistent increase in RMSE values was observed between DSM 1 m and 20 m resolution, yielding RMSE values from 1.302 to 7.175. Similarly, Figure 7 shows the image after orthorectification process based on different spatial resolution DSM such as a_1 with 31 cm and

(a)

(b)

(c)

(d)

(e)

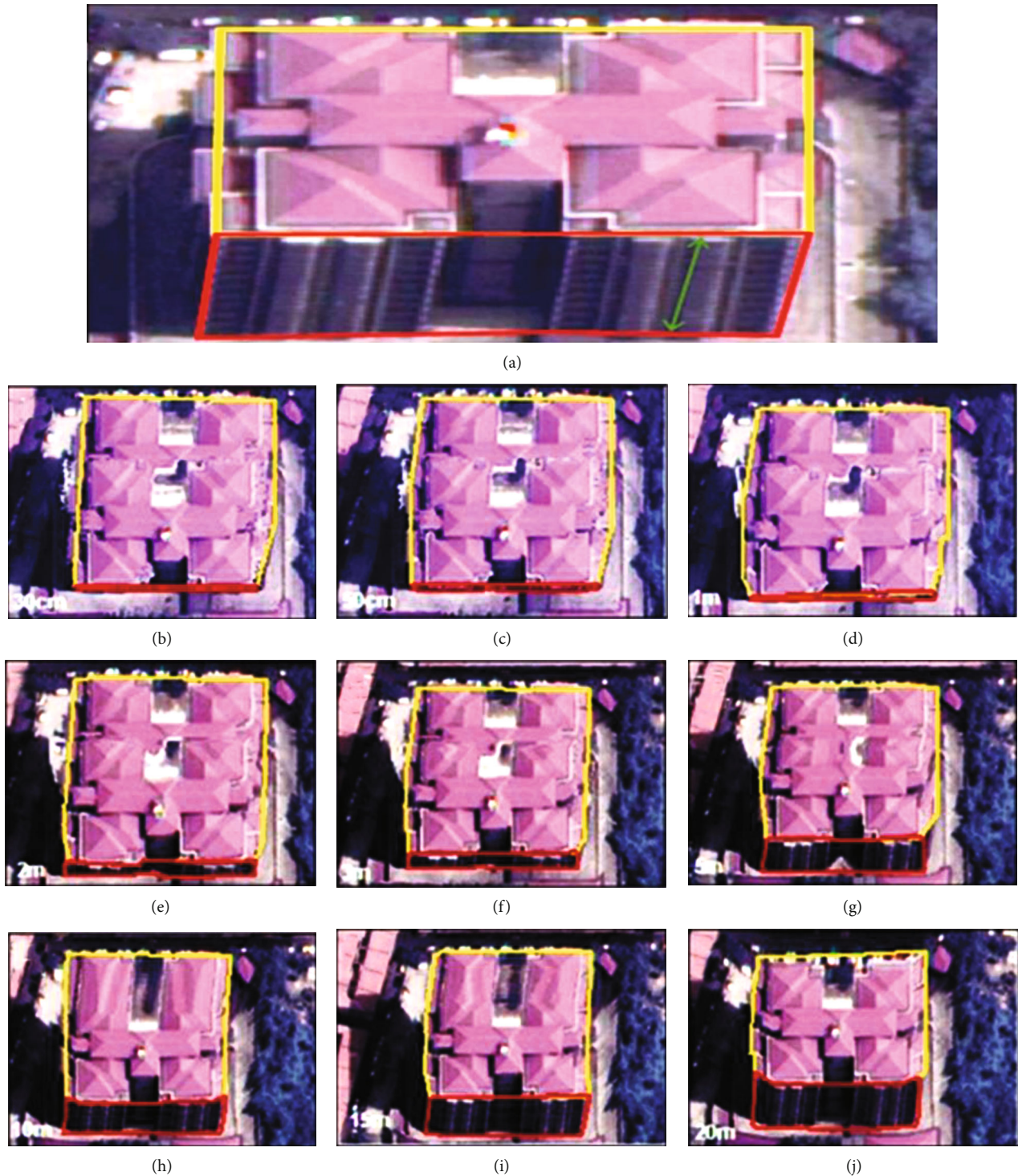(f)

(g)

(h)

(i)

(j)

FIGURE 8: (a) Leaning of the building prior to orthorectification; (b–j) image after the orthorectification process and the effects of DSM accuracy on the building lean.

a_2 with DSM 50 cm. The experimental results consistently yielded the most accurate values for validating the GCPs of the orthoimage based on 30 cm DSM in orthoimages. Thus, the accuracy of the orthoimages was improved reasonably based on DSM data.

The RPC orthorectification model was applied to the WorldView-3 image based on the free source DEM of 30 m (SRTM). The result obtained indicated the highest RMSE value of 7.947 compared with the orthoimage, which was obtained from high-resolution DSM of 31 cm (RMSE = 0.638). The significant difference between the DSM (31 cm) and the DEM (SRTM) (30 m) results indicated a unique relationship between the DEM or DSM accuracy and orthorectification accuracy.

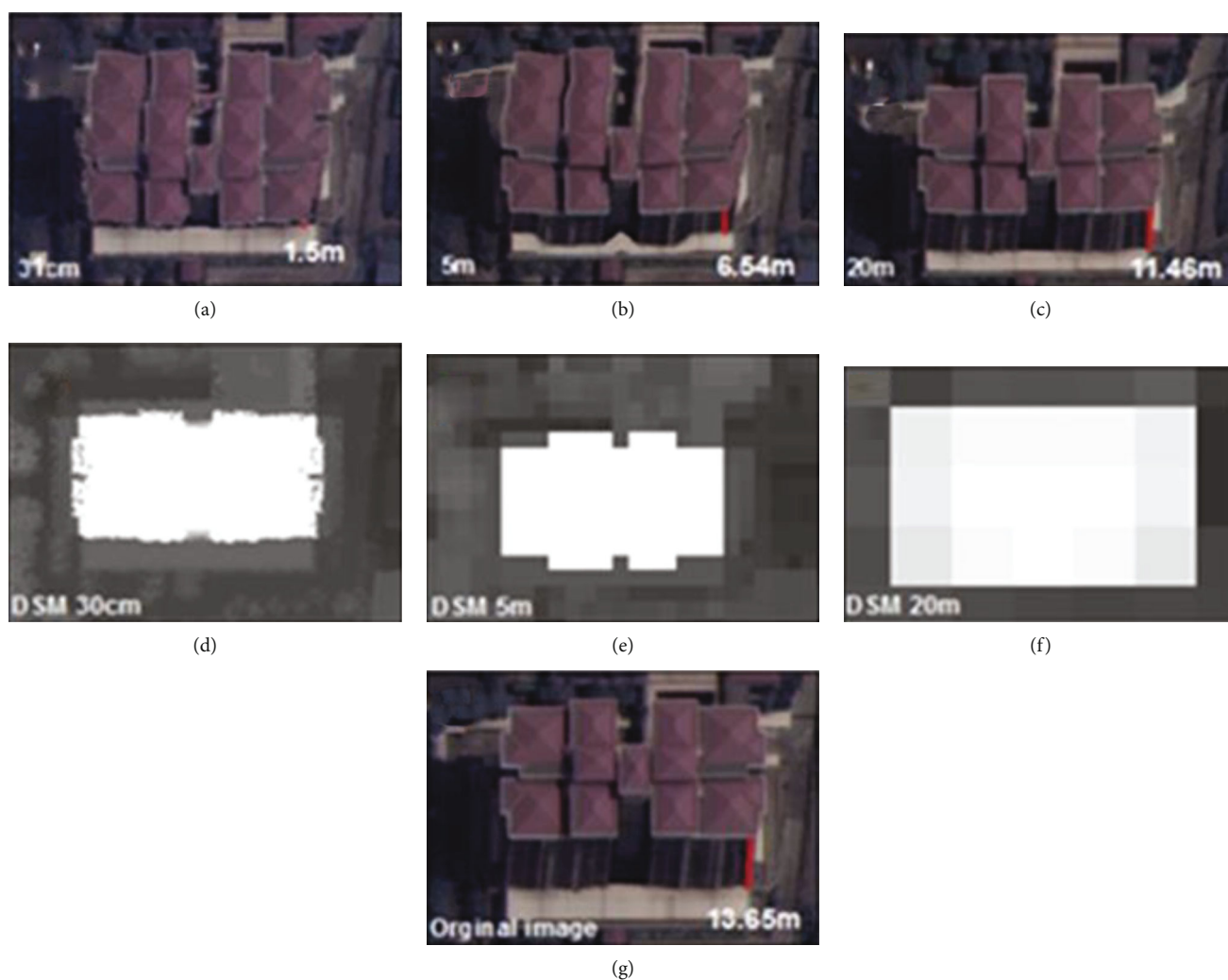(a)

(b)

(c)

(d)

(e)

(f)

(g)

Figure 9: (a–f) Relation between DSM resolution and leaning of building; (g) image prior to the orthorectification process.

According to the results obtained, the final optimal DSM of the orthorectification process was 31 cm resolution, which showed the least RMSE value. The high-resolution DSM and GCPs derived from high-resolution DEM combined in the proposed model (RPC orthorectification model) reduced the RMSE of the orthorectification of the final result to 0.638 m compared with the 1.07 m achieved by Zhang et al. [1], who developed a model based on the combination of RPCs and the Spline Function Model and using DEM SRTM at 30 m. The orthorectification model was applied different times to produce various orthoimages. Each orthoimage showed different horizontal distortions and building lean effects. Therefore, increasing the DSM resolution increased the accuracy level of the orthoimages, whereas distortion and building lean effects were decreased, as shown in Figure 8. Additionally, our proposed was also applied for the orthorectification process on the scenario image (Figure 8) based on a varying resolution of DSM form 31 cm to 20 m.

The final results revealed that building lean and DSM accuracy are highly related. The original building lean was 13.65, which decreased to 11.46 after applying orthorectifi-

Table 2: Sample of horizontal distortion in buildings with height of 91–120 m.

Type of DSM	Horizontal distortion
Original image prior to orthorectification	13.5–14.5
DSM 30 cm	1.31–1.4
DSM 50 cm	1.41–1.6
DSM 1 m	2.51–3.00
DSM 2 m	3.51–4.00
DSM 3 m	5.01–5.8
DSM 5 m	8.01–10.00
DSM 10 m	9.41–11.30
DSM 15 m	10.61–12.20
DSM 20 m	10.81–12.40

cation to the building at DSM of 20 m. Figure 9 shows the details of the results obtained after orthorectification.

Therefore, developing an approach to present a table-based ranking that compares the accuracy of the same image obtained from orthorectification and GCP with different
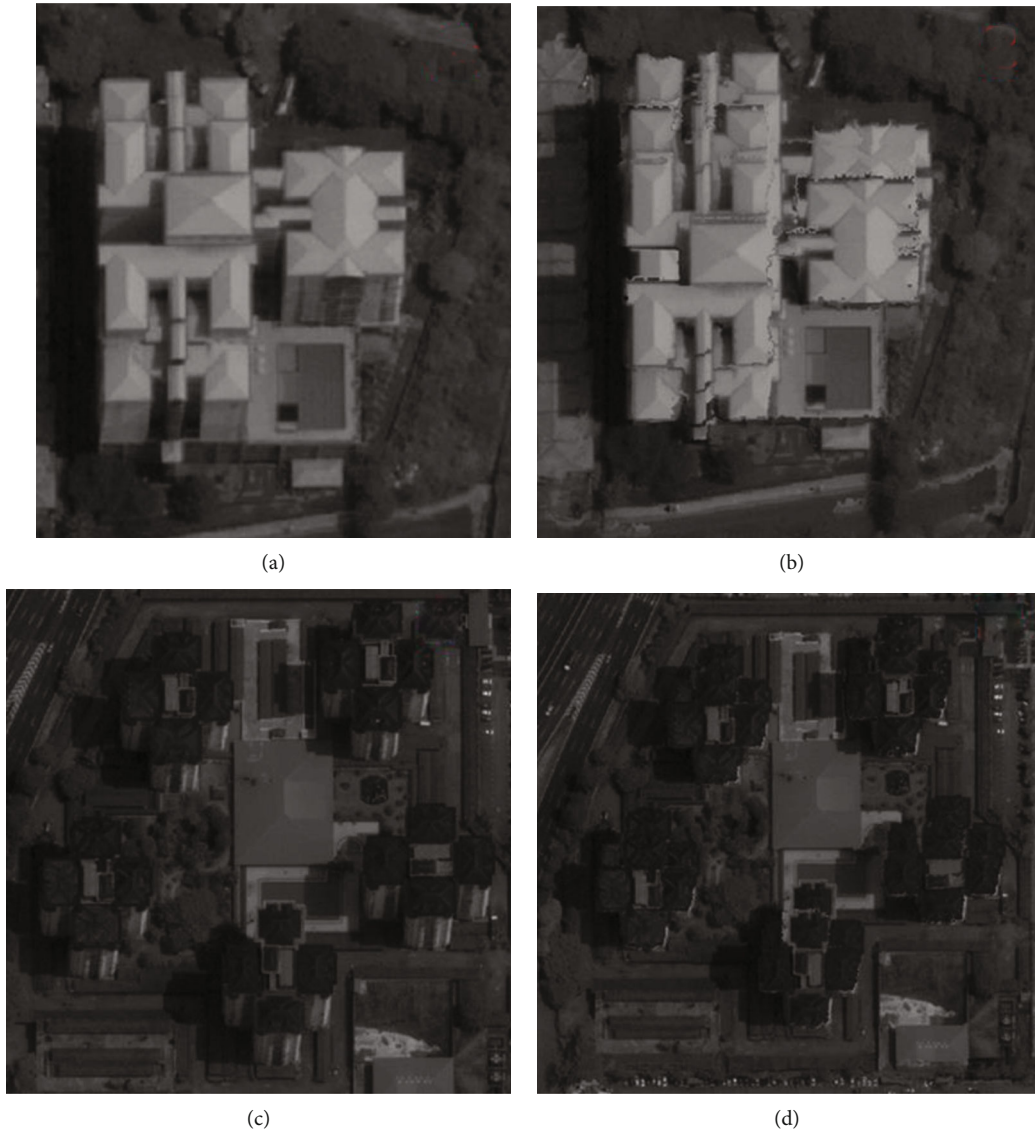
(a)

(b)

(c)

(d)

FIGURE 10: Leaning of the building prior to orthorectification based on DSM 0.30 cm whereas (a, c) before orthorectification and (b, d) after orthorectification.

DSM resolutions is necessary. This approach would provide clear information for future analysis and development. LiDAR point clouds with very high spatial resolution were used to produce a very high-resolution DEM. Thus far, no available criterion has been provided regarding the best DEM data. Improved image orthorectification result could be achieved if DEM data with high spatial resolution are available for orthorectifying images. The increased DSM resolution indicated the decreased error in the horizontal distortion of high buildings (>30 m). For instance, for a building height of 91–120 m, the horizontal distortion was measured and is shown in Table 2. Additionally, Figure 10 shows the leaning of the building prior to orthorectification based on DSM 0.30 cm, where it can be observed that the building height at *A* is 95 m and at *C* is between 109 and 116 m and the horizontal distortion is between 1.33 and 1.36.

4. Conclusions

LiDAR-derived GCPs and different DSM resolutions (31 and 50 cm and 1, 2, 3, 5, 10, 15, and 20 m) were proposed for image orthorectification. LiDAR data were used to obtain high-ability GCPs and DSM at the increased accuracy required for photogrammetry and orthorectification. The final image demonstrated the advantage of LiDAR-based GCPs with high-resolution DSM in producing high-quality orthoimages with an accuracy of 0.638 m. The accuracy of the orthorectified image was improved by increasing GCPs to more than the usual value. The comparison between final results indicated that the optimal orthoimage was selected based on the best accuracy of the final results, depending on the optimal images. Moreover, the optimal DSM used in orthorectification with the WV-3 image was DSM resolution of 31 cm. The orthorectification applied on WV-3

multispectral image resolution was 1 m, and the optimal DSM was 1 m. Furthermore, the correlation between horizontal distortion and DSM resolution was identified. The increased accuracy led to decreased horizontal distortion. The developed advanced remote sensing data allowed the generation of GCPs and was useful in the event of limited access to field surveys. Therefore, it can be said that a better result for image orthorectification may be expected with higher spatial resolution; especially, DSM was produced from airborne laser-scanning, which provides a very useful source of information for 3D building reconstruction. The orthorectified images increased the quality of land use and land cover used in many fields. Therefore, the proposed methodology will provide a useful tool to aid decision-makers in selecting the best LiDAR for orthorectification. With the wide range of application of high-resolution satellite imagery, using existing commercial image processing packages, the development of operational and efficient satellite image processing procedures such as high accurate image orthorectification will benefit those users who have a limited knowledge of remote sensing image processing. Finally, our method has been proven to be applicable to correct significant geometric distortions present on test image sets.

Data Availability

The data used in this study can be available from the corresponding author.

Conflicts of Interest

The authors declare no conflict of interest.

Acknowledgments

References

[1] H. Zhang, R. Pu, and X. Liu, "A new image processing procedure integrating PCI-RPC and ArcGIS-Spline tools to improve the orthorectification accuracy of high-resolution satellite imagery," *Remote Sensing*, vol. 8, no. 10, p. 827, 2016.

[2] N. Joshi, M. Baumann, A. Ehammer et al., "A review of the application of optical and radar remote sensing data fusion to land use mapping and monitoring," *Remote Sensing*, vol. 8, no. 1, p. 70, 2016.

[3] S. Abdullahi and B. Pradhan, "Sustainable brownfields land use change modeling using GIS-based weights-of-evidence approach," *Applied Spatial Analysis and Policy*, vol. 9, no. 1, pp. 21–38, 2016.

[4] R. Bridgelall, J. B. Rafert, and D. Tolliver, *Remote Sensing of Multimodal Transportation Systems*, Mountain Plains Consortium, Colorado State University, 2016.

[5] E. Symeonakis, K. Petroulaki, and T. Higginbottom, "Landsat-based woody vegetation cover monitoring in southern African savannahs," *ISPRS - International Archives of the Photogrammetry, Remote Sensing and Spatial Information Sciences*, vol. XLI-B7, pp. 563–567, 2016.

[6] Y. Peng, R. B. Kheir, K. Adhikari et al., "Digital mapping of toxic metals in Qatari soils using remote sensing and ancillary data," *Remote Sensing*, vol. 8, no. 12, 2016.

[7] J. Rodriguez, S. Ustin, S. Sandoval-Solis, and A. T. O'Geen, "Food, water, and fault lines: remote sensing opportunities for earthquake- response management of agricultural water," *Science of the Total Environment*, vol. 565, pp. 1020–1027, 2016.

[8] J.-P. Jhan, J.-Y. Rau, and C.-Y. Huang, "Band-to-band registration and ortho-rectification of multilens/multispectral imagery: a case study of MiniMCA-12 acquired by a fixed-wing UAS," *ISPRS Journal of Photogrammetry and Remote Sensing*, vol. 114, pp. 66–77, 2016.

[9] E. P. Baltsavias, "Object extraction and revision by image analysis using existing geospatial data and knowledge: state-of-the-art and steps towards operational systems," *ETH Zurich*, vol. XXXIV, Part 2, 2002.

[10] Y. Hu and C. V. Tao, "Updating solutions of the rational function model using additional control information," *Photogrammetric Engineering and Remote Sensing*, vol. 68, no. 7, pp. 715–724, 2002.

[11] J. S. Evans and A. T. Hudak, "A multiscale curvature algorithm for classifying discrete return LiDAR in forested environments," *IEEE Transactions on Geoscience and Remote Sensing*, vol. 45, no. 4, pp. 1029–1038, 2007.

[12] X. Liu, Z. Zhang, J. Peterson, and S. Chandra, "LiDAR-derived high quality ground control information and DEM for image orthorectification," *GeoInformatica*, vol. 11, no. 1, pp. 37–53, 2007.

[13] O. R. Belfiore and C. Parente, "Comparison of different algorithms to orthorectify WorldView-2 satellite imagery," *Algorithms*, vol. 9, no. 4, p. 67, 2016.

[14] T. Prakash, B. Comandur, T. Chang, N. Elfiky, and A. Kak, "A generic road-following framework for detecting markings and objects in satellite imagery," *IEEE Journal of Selected Topics in Applied Earth Observations and Remote Sensing*, vol. 8, no. 10, pp. 4729–4741, 2015.

[15] I. Henrico, L. Combrinck, and C. Eloff, "Accuracy comparison of Pléiades satellite ortho-images using GPS device based GCPs against TerraSAR-X-based GCPs," *South African Journal of Geomatics*, vol. 5, no. 3, pp. 358–372, 2016.

[16] T. G. Whiteside and R. E. Bartolo, "Mapping aquatic vegetation in a tropical wetland using high spatial resolution multispectral satellite imagery," *Remote Sensing*, vol. 7, no. 9, pp. 11664–11694, 2015.

[17] D. Chaudhuri, N. K. Kushwaha, A. Samal, and R. Agarwal, "Automatic building detection from high-resolution satellite images based on morphology and internal gray variance," *IEEE Journal of Selected Topics in Applied Earth Observations and Remote Sensing*, vol. 9, no. 5, pp. 1767–1779, 2016.

[18] J. T. Kerr and M. Ostrovsky, "From space to species: ecological applications for remote sensing," *Trends in Ecology & Evolution*, vol. 18, no. 6, pp. 299–305, 2003.

[19] D. Vlasic, P. Peers, I. Baran et al., "Dynamic shape capture using multi-view photometric stereo," in *ACM SIGGRAPH Asia 2009 papers*, pp. 1–11, 2009.

[20] J. Grodecki and G. Dial, "IKONOS geometric accuracy," in *Proceedings of joint workshop of ISPRS working groups I/2, I/5 and IV/7 on high resolution mapping from space*, pp. 19–21, 2001.

[21] J. E. Nichol, A. Shaker, and M.-S. Wong, "Application of high-resolution stereo satellite images to detailed landslide hazard assessment," *Geomorphology*, vol. 76, no. 1-2, pp. 68–75, 2006.

[22] E. Widyaningrum, M. Fajari, and J. Octariady, "Accuracy comparison of vhr systematic-ortho satellite *imageries* against vhr orthorectified imageries using GCP," *International Archives of the Photogrammetry, Remote Sensing & Spatial Information Sciences*, vol. XLI-B1, pp. 305–309, 2016.